Jupiter's zonal winds and their variability studied with small-size telescopes

N. Barrado-Izagirre, J. Rojas, R. Hueso, A. Sanchez-Lavega, F. Colas, J. Dauvergne, D. Peach, Iopw Team

Astronomy
& Astrophysics

Jupiter's zonal winds and their variability studied with small-size telescopes[⋆],[⋆⋆]

N. Barrado-Izagirre[1,2], J. F. Rojas[2,3], R. Hueso[1,2], A. Sánchez-Lavega[1,2], F. Colas[4], J. L. Dauvergne[5], D. Peach[6], and the IOPW Team[⋆⋆⋆]

[1] Departamento Física Aplicada I, Universidad del País Vasco UPV/EHU, ETS Ingeniería, Alameda Urquijo s/n, 48013 Bilbao, Spain
e-mail: naiara.barrado@ehu.es
[2] Unidad Asociada Grupo Ciencias Planetarias UPV/EHU-IAA (CSIC), 48013 Bilbao, Spain
[3] Departamento Física Aplicada I, Universidad del País Vasco UPV/EHU, EUITI, Alameda Urquijo s/n, 48013 Bilbao, Spain
[4] Institut de Mécanique Céleste et de Calcul des Ephémérides, Observatoire de Paris, UMR 8028 CNRS, 77 av. Denfert-Rochereau, 75014 Paris, France
[5] S2P – Station de Planétologie des Pyrénées, 65200 La Mongie, France
[6] British Astronomical Association, Burlington House, Piccadilly, London W1JODU, UK

ABSTRACT

Context. The general circulation of Jupiter's atmosphere at cloud level is dominated by a system of zonal jets that alternate in direction with latitude. The winds, measured in high-resolution images obtained by different space missions and the *Hubble* Space Telescope, are overall stable in their latitude location with small changes in intensity at particular jets. However, the atmosphere experiences repetitive changes in the albedo of particular belts and zones that are subject to large-scale intense disturbances that may locally influence the profile.
Aims. The lack of high-resolution images has not allowed the wind system to be studied with the regularity required to assess its stability with respect to these major changes or to other types of variations (e.g., seasonality). To amend that, we present a study of the zonal wind profile of Jupiter using images acquired around the 2011 opposition by a network of observers operating small-size telescopes with apertures in the range $0.20-1$ m.
Methods. Using an automatic correlation technique, we demonstrate the capability to extract the mean zonal winds in observing periods close to the opposition. A broad collaboration with skilled amateur astronomers opens the possibility to regularly study short- and long-term changes in the jets of Jupiter.
Results. We compare the 2011 Jovian wind profile to those previously obtained. The winds did not experience significant short-term changes over 2011 but show noteworthy variations at particular latitudes when compared with wind profiles from previous years. Most of these variations are related to major changes in the cloud morphology of the planet, in particular at $7°$ N where an intense eastward jet varies around 40 ms^{-1} in its intensity according to the development or not of the "dark projection" features, confirming previous results.

Key words. planets and satellites: atmospheres – techniques: image processing – telescopes

1. Introduction

The planet Jupiter has the largest and most dynamic atmosphere in our solar system. Its general circulation at visible wavelengths is dominated by a system of zonal wind jets that alternate in latitude, reach peak values from -50 ms^{-1} (westward) to 160 ms^{-1} (eastward), and whose latitudinal extent correlates with the well-defined system of dark bands and bright zones (Vasavada & Showman 2005; Ingersoll et al. 2004). Explaining the origin of the structure of the wind system from a dynamical point of view remains a major challenge (Ingersoll et al. 2004). Prominent and unexplained features of the wind system are: 1) the broad nearly symmetric eastward equatorial zonal jet,

which is relatively similar to the equatorial jet structure of Saturn (Sánchez-Lavega et al. 2000; García-Melendo et al. 2011b) but unlike the atmospheric westward equatorial and tropical circulation of Earth, Uranus, or Neptune (Sromovsky et al. 2001, 2009); 2) the overall symmetry of the zonal jets broken at some latitudes by the presence of large-scale vortices like the Great Red Spot (Beebe et al. 1989; Rogers 1995; Simon-Miller et al. 2012); 3) higher wind velocities appear on the eastward jets, as they do in Saturn but not in Uranus and Neptune.

Relevant questions about the observed wind system, which is measured at the $0.5-1$ bar altitude level tracking the motions of small-cloud features, are: how deep it extends (shallow or deep relative to the planetary radius) (Dowling & Ingersoll 1989; Dowling 1995; Ingersoll et al. 2004; Vasavada & Showman 2005; Sánchez-Lavega et al. 2008), if winds are variable or not (García-Melendo & Sánchez-Lavega 2001; Asay-Davis et al. 2011; Simon-Miller et al. 2007; Simon-Miller & Gierasch 2010), and if the zonal jets support cyclic variations as has been claimed (Simon-Miller et al. 2007). The study of long- or short-term global wind variations is fundamental to these questions and to

---

Table 1. Summary of global wind measurements in Jupiter at visible wavelengths.

Year (period)	Facility	Approx. maximum resolution (km/pixel)	Reference
1979	Voyager 1 & 2 ISS[1]	100	Limaye (1986)
1995−98	HST WFPC2[2]	140	García-Melendo & Sánchez-Lavega (2001)
2000	Cassini ISS[1]	120	Porco et al. (2003)
			Vasavada & Showman (2005)
			García-Melendo et al. (2011a)
			Asay-Davis et al. (2011)
2008	HST WFPC2[2]	160	Asay-Davis et al. (2011)
2011	IOPW team	380	This work

Notes. [1] ISS: imaging Science Subsystem, [2] WFPC2: wide Field Planetary Camera 2.

determine which is the energy source behind the atmospheric circulation (solar or internal or both).

The meridional structure of the zonal winds had been well established from ground-based observations over the XXth century and was based in long-term tracking of long-lived well-contrasted features (Peek 1958; Rogers 1995). However, the details of the global structure of the wind system remained obscure until the Voyager 1 and 2 flybys in 1979, which produced the first set of precise measurements of the zonal winds of Jupiter (Limaye 1986). In 1995, in situ measurements by the *Galileo* probe (Atkinson et al. 1998) and observations from the *Galileo* orbiter (Vasavada et al. 1998) led to new precise measurements of the winds on some localized areas, but did not result in a complete wind profile. Images acquired by the *Hubble* Space Telescope (HST) were used to obtain several profiles on different dates from 1995 to 2000 (García-Melendo & Sánchez-Lavega 2001). The Cassini flyby of Jupiter in late 2000 provided high-resolution images that were also used to study the zonal winds system (Porco et al. 2003; Vasavada & Showman 2005). The New Horizons flyby of Jupiter in 2007 also provided valuable data of Jupiter's atmospheric dynamics (Reuter et al. 2007), but an analysis of the global wind profile over this dataset has not yet been published. The latest Jupiter overall wind profile was measured using HST observations acquired in 2008 (Asay-Davis et al. 2011). A summary of the characteristics of these observations and wind retrievals is given in Table 1.

Considering the results of these studies as a whole, there have been very few changes since the early measurements by the Voyagers to the latest wind fields from HST observations in 2008. The mean intensity of the winds has shown temporal variability on the order of ~10 ms^{-1} (Asay-Davis et al. 2011) and a remarkable stability of the latitudes of the zonal jets' maximum velocities. Although some of the bands' morphology changes in periods of years (Peek 1958; Chapman & Reese 1968; Reese 1972; Minton 1972a,b; Smith & Hunt 1976; Sánchez-Lavega & Rodrigo 1985; Rogers 1995; Sánchez-Lavega & Gómez 1996; Sánchez-Lavega et al. 1996; Fletcher et al. 2011; Pérez-Hoyos et al. 2012), the wind profile maintains a remarkable temporal stability. Furthermore, this zonal wind profile is not strongly affected by the dynamic perturbations at cloud level, such as those developed by convective storms like the South Equatorial Belt Disturbance (SEBD; Sánchez-Lavega et al. 1996; Sánchez-Lavega & Gómez 1996) and the North Temperate Belt Disturbance (NTBD) (García-Melendo et al. 2005, 2009; Sánchez-Lavega et al. 2008; Barrado-Izagirre et al. 2009a). Even large impacts on the planet such as those of 1994 and 2009

(Hammel et al. 1995, 2010; Sánchez-Lavega et al. 1998, 2010), which released energies at the impact's locations of 10^{22} and 10^{20} joules, respectively, were not able to alter the winds at the latitudes of the impacts. Nevertheless, there have been some changes in the zonal winds of Jupiter that seem to be related to the morphology of the Jovian clouds. The most conspicuous changes happen occasionally in the North Equatorial Belt (NEB), in the South Equatorial Belt (SEB), and in the North Temperate Belt (NTB). The changes in the NEB, for example, may be linked to the appearance of large-scale hot spots (García-Melendo et al. 2011a) and those in the SEB to zonal distribution of chevrons and waves (Simon-Miller et al. 2012). There are also some local changes in the NTB and in the westward 17°N (planetocentric) jet (Barrado-Izagirre et al. 2009a) that seem to be linked to planetary-size disturbances.

Up to now Jupiter zonal wind profiles at cloud level have been measured either by using either very high-resolution observations, attainable only from HST or spacecraft missions, or by performing detailed tracking of selected features over a long period to determine their motions with enough accuracy. The latter procedure is only applicable to relatively large-scale structures that survive over many days, and although it provides accurate zonal drifts, it lacks latitudinal spatial resolution to resolve the structure of the jets. Typical precision of wind retrievals from ground-based data spanning a few weeks can be 1 ms^{-1}, but the latitudinal precision may be only 0.5−1° and the wind retrievals may lack details on many different latitudes. Wind studies based on HST data over one or two rotations can reach precisions on the order of 10 ms^{-1} (García-Melendo & Sánchez-Lavega 2001) with a latitudinal incertitude of 0.25°. Spacecraft flybys have provided wind retrievals accurate to 6−11 ms^{-1} (Asay-Davis et al. 2011) with latitudinal precisions of 0.1° or better.

However precise, spacecraft data represent only the dynamic state of the planet in a few epochs (1979, 2000, and 2007 from the Voyagers, *Cassini*, and New Horizons flybys, respectively). In addition the HST data is too scarce to study short-time and cyclic variations that present many gaps in several years. Fortunately, recent advances in imaging techniques have allowed diffraction-limited images of bright objects to be obtained with small telescopes applying the principle of "lucky imaging" (Law et al. 2006). This technique is based on selecting the best quality images from a stream of frames obtained by high-sensitivity electronic detectors. Each frame is blurred differently due to atmospheric seeing. Specialized software (such as Registax[1]) is used to automatically select the best frames that coregister and

---

[1] http://www.astronomie.be/registax/

stack a final image of high signal-to-noise ratio and reduced blurring. In good seeing conditions, telescopes with diameters in the range of ~20−50 cm provide images that attain their diffraction limit; this translates into spatial resolutions of 1500−600 km over the Jovian disk at opposition (Parker 2007). The large number of amateur astronomers observing Jupiter provides a nearly continuous monitoring of the planet. Selecting the best images obtained close to opposition by observers from different locations on Earth, we can find high-quality Jupiter images of the same area obtained after one or two Jupiter rotations. These images can yield wind retrievals with a precision reaching 7 m/s and with a latitudinal precision of 0.2−0.3°, depending on the image quality and the latitudes examined.

Previous studies using these kinds of images (García-Melendo et al. 2009, 2011a; Barrado-Izagirre et al. 2009a; Sánchez-Lavega et al. 2008, 2011; Pérez-Hoyos et al. 2012) inferred wind velocities by manual tracking of long-lived cloud details, which had been tracked over many different images or image pairs separated by several planetary rotations. We show that an automatic cloud correlation technique such as those used to analyze higher resolution HST or spacecraft data also works for ground-based observations with small telescopes obtained by keen amateur observers. Using these observations it is possible to retrieve Jovian wind profiles regularly at the small cost of a slightly larger uncertainty. This opens the possibility to study regularly short- and long-term as well as cyclic changes in the jet streams of Jupiter.

In this paper we present the wind retrieval method and our results for different periods of time in late 2011, in addition to discussing the long-term stability of the winds system. Section 2 describes the observations and the methods used to take them. In Sect. 3 we discuss the methodology to analyze the images and measure winds. The main results of this work are presented in Sect. 4. Firstly, we discuss the morphology of the planet, its appearance, and the meteorological phenomena present in the visible cloud deck as well as present the resulting mean wind profile for late 2011. Secondly, we present an analysis of the variability of the winds in Jupiter considering long-term and short-term variability. Finally, we give our conclusions in Sect. 5.

2. Observations

The atmosphere's node of the International Outer Planet Watch (IOPW) manages an open access database of outer planet images called Planetary Virtual Observatory (PVOL[2]) which is documented in Hueso et al. (2010). It currently stores a large number of images (more than 15 500 of Jupiter and Saturn) that have been mainly contributed by an international network of amateur astronomers and by some planetary scientists. Most of the amateur observations come from telescopes with diameters in the range of 25−40 cm. The IOPW-PVOL observations have a wide temporal coverage starting from the year 2000. The spatial resolution, overall quality of the images and the number of observers contributing to this database are improving year after year (the number of Jupiter observations per year doubles every four years and reached 2600 individual observations in 2011).

The quality of the original images acquired by amateur astronomers is very variable. Globally it obviously depends on the date of the observation with respect to Jupiter opposition, when the planet reaches its maximum size on the sky and zero phase angle. It also depends on variables related to the observer and
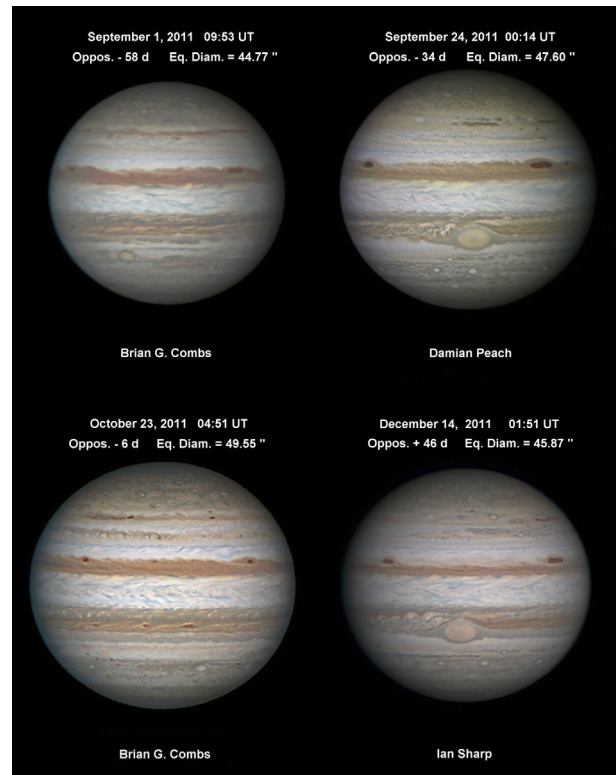
Fig. 1. Examples of Jupiter images in 2011 used in this study. Data and observers are indicated. We note the different apparent size of Jupiter due to the separation from the opposition date that occurred on October 29, 2011.

atmospheric conditions: telescope diameter, optical quality, collimation, overall equipment (camera, magnification lenses, filters), image processing methods, planet altitude at the latitude of the observer, and the atmospheric seeing. A large amateur telescope (typically a 14-inch Schmidt-Cassegrain) of 354 mm aperture has a diffraction limit of 0.4 arcsec, as stated by the angle at which the minimum in the diffraction pattern of a circular aperture occurs:

$$\sin \theta \approx 1.22 \frac{\lambda}{d}, \tag{1}$$

where θ is the angular resolution, λ is the wavelength of light, and d is the diameter of the telescope's aperture. For this telescope, taking a mean distance between Jupiter and the Earth of approximately 6.26×10^8 km from September to December 2011, the diffraction-limited spatial resolution over the Jovian disk is about 1200 km (0.95° of longitude).

Although most of the contributions to the IOPW-PVOL database come from amateurs, there are also observations obtained by professional observatories. In particular we used images from the Pic-du-Midi 1050 mm telescope with a diffraction limit of 0.13 arcsec at red wavelengths translating into maximum spatial resolutions of 0.3°/pixel (381 km/pixel over Jupiter's disk at opposition).

Images used in this work are red green blue (RGB) color compositions obtained in broadband filters and processed from video observations to get a single jpg file, which is the result of a strong contrast enhancement. A video observation of the planet with hundreds or thousands of frames is used to build a stacked high signal-to-noise ratio image, which is processed with different high-pass or wavelet filters to increase the contrast of small cloud features. Due to the contrast enhancement of the images,

---

[2] http://www.pvol.ehu.es/pvol/

they cannot be absolutely calibrated in reflectivity; however, this is not a problem when using the images for dynamical studies, which is our purpose in this work. Figure 1 shows four Jupiter observations obtained by different observers close to Jupiter opposition in 2011. Changes in image size correspond to the apparent size of the planet as the dates approached and departed from the opposition date on October 29, 2011.

We searched for pairs of high-quality comparable images separated by one or two Jupiter rotations that show the same Jovian longitude range. Image pairs separated by more than 20 h are not usable because of large changes in the cloud patterns. In a few cases we identified image trios that consist of three images, with each image separated from the others by 10 h so that the first one and the last one are also two rotations apart. These images provided the best results because the large time difference minimizes measurement errors. Our selection criteria resulted in a selection of 52 high-quality images from September to December 2011 from roughly 1700 available images near the opposition of Jupiter. Table 2 summarizes these images and the observers that acquired them.

3. Methodology and analysis

Image pairs were selected according to their quality and time separation. The RGB images were transformed into gray-scale images with a principal component analysis algorithm, which ensures that the gray-scale image contains most of the spatial information and the minimum amount of noise (Petrou & Petrou 2010). The gray-scale images were navigated using the software LAIA (Cano 1998), which allows a pixel position (x,y) to be transformed on the image into longitude-latitude planetary coordinates (Barrey 1984). The orientation of the images is a critical factor for navigation since a small error in the tilt of the planetary axis introduces a noticeable error in the wind measurement; for instance, a tilt error of 1° translates into a zonal velocity error of 4 ms^{-1} at 30° of latitude for a 10 h image pair. The images were used to build cylindrical projections of the same longitude and latitude range. The projections provide a good method to check the accuracy of the determination of the planetary axis since images that are wrongly oriented result in cylindrical maps with tilted bands and zones and only accurately oriented images result in all bands and zones being perfectly horizontal. All the projections were obtained with a spatial resolution of 0.1°/pixel oversampling images within a factor ∼2.5−4 of their initial resolution. This resulted in uniform resolution of the maps, negligible single pixel noise, and better accuracy in wind determination by correlation since the pixel scale was magnified. At this scale a single pixel displacement over 10 h results in 3 ms^{-1} and smoothly varying wind profiles could be obtained (the error bars at each latitude are much larger than this 3 ms^{-1} scale, as will be discussed later).

The natural limb darkening of the images was corrected to properly compare similar regions in both images. Most of the observers apply image processing techniques that contrast the atmospheric details and reduce the natural limb darkening. However, those images where the limb darkening is visible were corrected using a Lambert function, a particular case of the Minnaert law (Minnaert 1941):

$$(I/F) = (I/F)_0 \cdot \mu^{k-1} \cdot \mu_0^k, \qquad (2)$$

where (I/F) is the observed reflectivity, $(I/F)_0$ is the corrected reflectivity, μ and μ_0 are the cosines of the viewing and illuminating angles (Horak 1950), and k is a limb darkening coefficient

that takes the value 1 for the Lambert correction. Further details of the procedure are given in Barrado-Izagirre et al. (2009b).

At this step both image maps can be compared using an image correlation algorithm that identifies common structures in both images. The correlation algorithm is detailed in Hueso et al. (2009) and is based on maximizing the cross-correlation of small sections of both images. In this case, instead of performing a correlation of the images in terms of two-dimensional windows, we modified the algorithm to perform a correlation of nearly zonal scans (very long and narrow boxes) that can be selected from the image and avoid problematic regions (with no features or transiting satellites or transiting shadows) and large-scale structures such as the great red spot (GRS), the oval BA or similar local weather patterns as shown in Fig. 2. Each wind measurement is assigned to the central latitude of the correlation window. Different implementations of zonal scans correlation techniques have been extensively used in studies of high-resolution images of Jupiter (Limaye 1986; García-Melendo et al. 2011a; Asay-Davis et al. 2011) but never before applied to amateur observations of the planet.

From the analysis of the selected 52 images, we retrieved about 21 500 wind vectors from which the obvious outliers (representing less than 2.5% of the total measurements) were removed. In some cases we verified the obtained results by manually tracking some of the visible cloud features over several images validating our technique.

Our final 21 000 wind vectors are distributed latitudinally as shown in Fig. 3. The number of measurements obtained in different latitudes depends on the cloud morphology. In the SEB and the south tropical zone (STrZ) we avoided areas close to the GRS, resulting in a lower density of wind vectors. In the NTB at 20° north, the relatively low number of vectors is due to the presence of the strong and narrow NTB jet, where the high meridional wind shear dissipates atmospheric details quickly.

Regarding the uncertainties involved in these wind measurements, we have to judge their sources. The main error source is the limited resolution of the images caused by the modest diameter of the telescopes. For image pairs separated by one-two planetary rotations (10−20 h), this factor alone translates into typical errors at equatorial latitudes of the order of ∼10−30 ms^{-1}. Additional sources of uncertainty come from small errors in the orientation of the planet axis and the image navigation. Errors in image orientation produce "skewed" wind profiles when compared with previously published wind profiles. There is also an uncertainty arising from the reference ellipse fitted to the planet disk to calculate the projection grid. In this case errors come from a misplaced ellipse with correct size or from an incorrect size ellipse. In both cases typical errors are of ±1 pixel that translates into errors comparable to those produced by the resolution of the images and that can be as large as 30 ms^{-1} in the worst cases for a 10 h image pair.

Another difficulty is that one or both of the images may have incorrect timing since the observation technique involves observations over times of a few minutes and the observers have their own methodology to assign a single time to their observations. Image pairs with incorrect timing result in wind velocity profiles shifted at all latitudes. In a typical 10 h image pair, a time uncertainty of 30 s translates into ∼10 ms^{-1} velocity shift. This is a very common problem when working with amateur images, which are typically RGB composites with each color channel built at a different but close time. In these cases we corrected the time difference to ensure that the zero-velocity or maximum velocity jets remain in the known positions. We first measure the wind profile and estimate its best fit using a reference wind
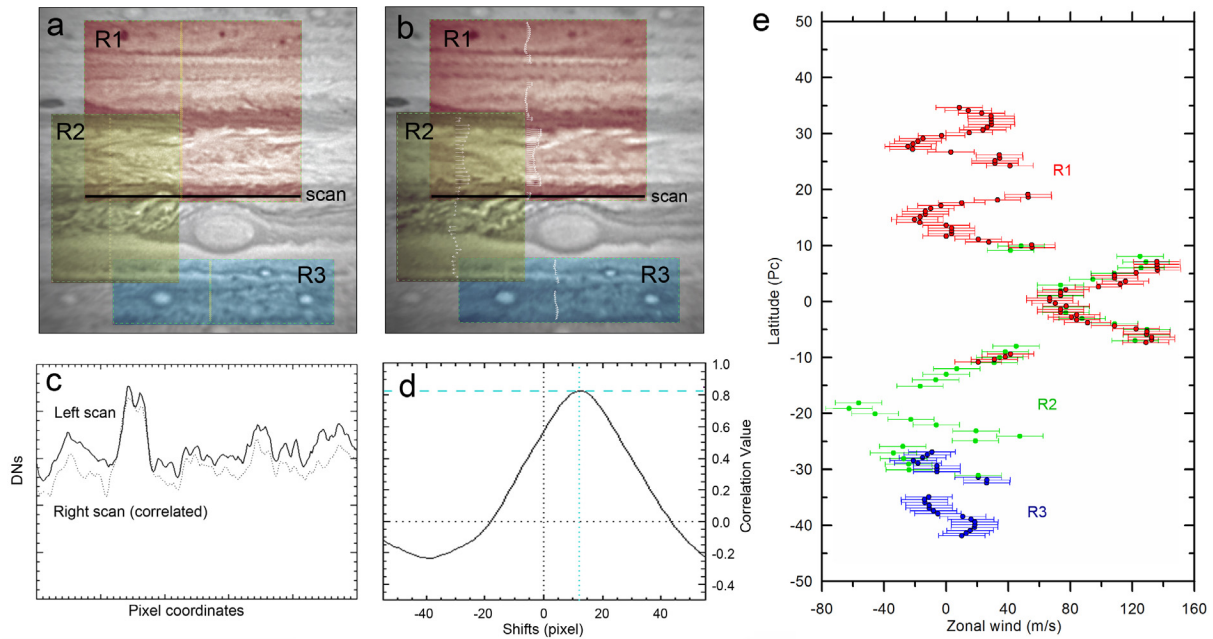
Fig. 2. Panels **a)** and **b)** show projected images obtained with a time separation of one planetary rotation. Regions where correlation scans were obtained are shaded areas labeled R1, R2, and R3. These regions were selected close to the central meridian of the original images, avoiding areas with large-scale features. Each region is decomposed in zonally long and latitudinally narrow stripes, which are compared with their equivalent latitudes in the second image with a correlation algorithm. The software draws wind vectors in each measurement. Panel **c)** shows a zonal scan (continuous line) on the R1 region in *the left panel* and its equivalent scan in the region R2 in *the right panel* (dashed line) after identifying the zonal shift that attains the maximum correlation between both scans. Panel **d)** shows the correlation function between these scans. Panel **e)** shows winds obtained in this image pair. Color codes correspond to measurements obtained in each region. Error bars here are 15 ms^{-1} from the spatial resolution and time separation.
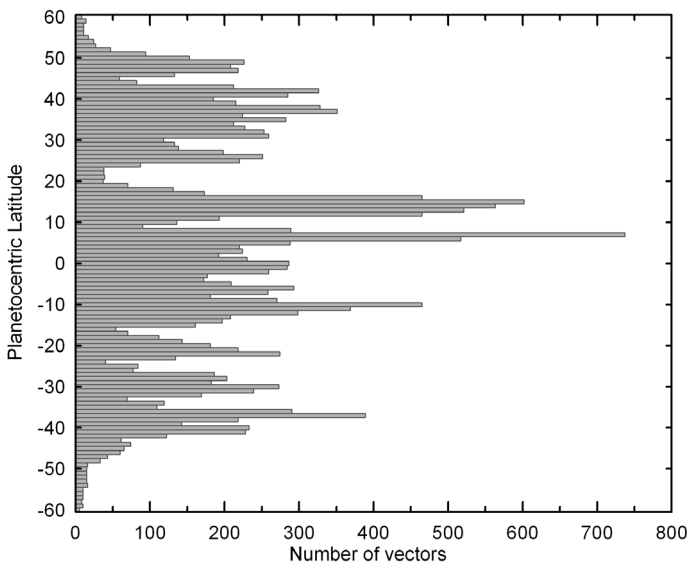
Fig. 3. Latitudinal distribution of the number of measured vectors.

profile. It is worth noting that the images we used are not derotated. This novel technique allows the observer to compensate for the shift of the details produced by the rotation of the planet while a video observation of the planet for several minutes is being taken. Derotation allows the signal-to-noise ratio of the final stacked image to be increased, resulting in an improvement of the spatial resolution of the observable details. It is a feature implemented in the popular WinJUPOS software used by many amateurs (Walker 2013)[3].

---

[3] http://jupos.org/gh/download.htm

From these error sources we consider that the minimum error value for each individual wind measurement is 15 ms^{-1}. To reduce the wind velocity error associated with each particular latitude bin, we need to measure several wind vectors. Moreover, the images were navigated and the winds measured independently by two of us to reduce the human errors associated with the navigation process. We averaged our wind measurements in latitude bins of 1° containing several measurements from the same or different image pairs. The standard deviation of the measurements in a bin typically resulted in error bars of 5 ms^{-1} for best latitudes and of 30 ms^{-1} for latitudes with large dispersion of vectors. There are some latitudes (especially high ones) with a small number of measurements per bin. In these cases, even when the standard deviation of the bin values is low, we consider a minimum 15 ms^{-1} error bar.

4. Results and discussion

Before discussing our wind results, it is worthwhile to discuss the particular morphology of the planet observed during the time period covered by the images analyzed.

4.1. Jovian cloud morphology in the September–December 2011 period

The cloud morphology during the period of wind measurements is shown in Fig. 4. Concerning the main Jovian belts and zones (between latitudes ±35°), we note the following (see also Fig. 2): (1) the South Temperate Belt was faded, except for a turbulent sector extending about 80° in longitude, with a detached oval BA characterized by its ringed structure and the accompanying small, dark cyclone and short turbulent area; (2) there was
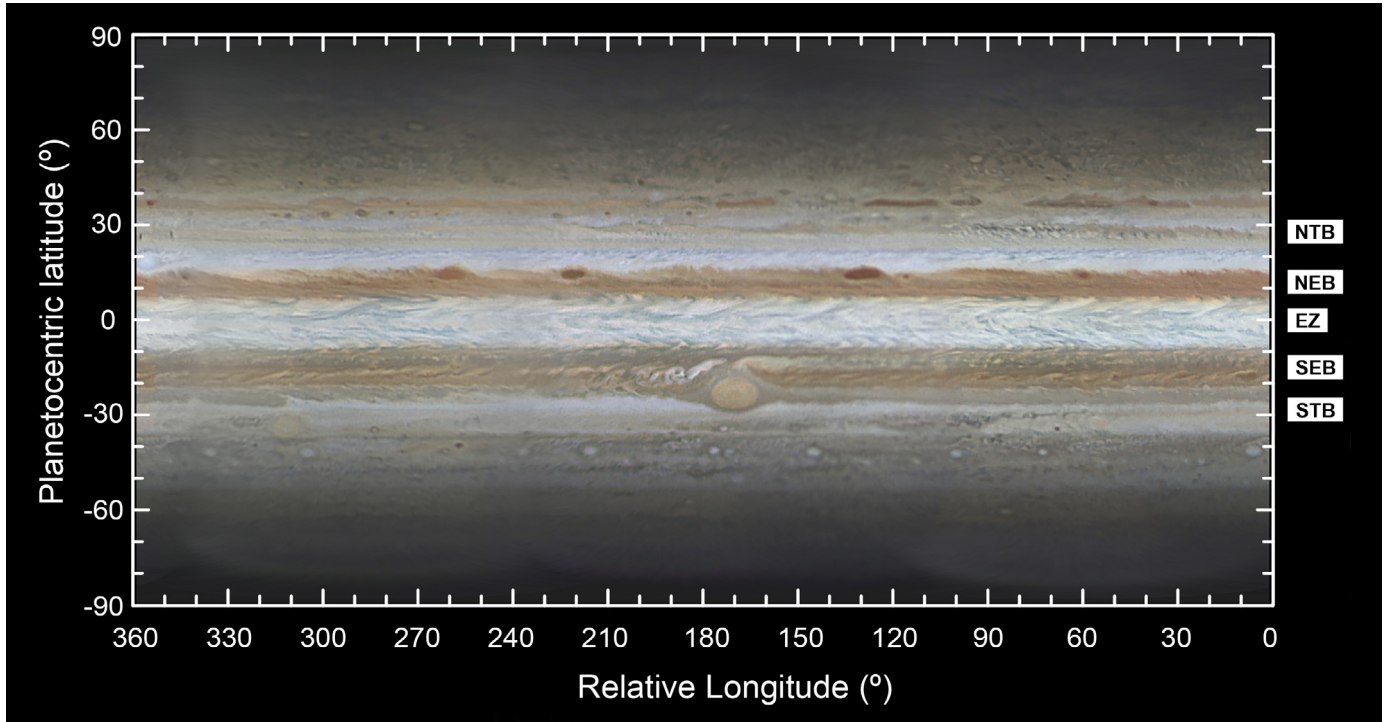
Fig. 4. Cylindrical map projection showing the general morphology of Jupiter in October 2011. The images for the composite were acquired from October 10 to 15 by J. L. Dauvergne, E. Rousset, E. Meza, P. Tosi, and F. Colas using the 1 m telescope at the Pic du Midi observatory.

a well-developed gray belt in the STrZ contiguous to the SEB, making this belt appear wider in latitude than it usually is; (3) the SEB was fully recovered as a low albedo band from its last fade (Pérez-Hoyos et al. 2012); (4) no large and conspicuous "dark projections" were present at the equatorward edge of the NEB (these are the low-albedo visible counterparts to the 5-μm hot spots; Arregi et al. 2006). We show that this is an important aspect affecting the wind profile; (5) on the NEB poleward side, three large barges dominate the scene (about five in total were present); (6) the north tropical zone (NTrZ) was a prominent zone, but the NTB was faint with small-scale features.

### 4.2. Mean Jovian wind profile

Jupiter opposition was on October 29, 2011, and from September to December 2011 we analyzed image pairs grouped in three periods or in a single global set representative of the mean wind profile for 2011. In total we considered 23 image pairs plus nine individual images for long-period tracking of particular features. Figure 5 shows the mean zonal wind for 2011. This wind profile is tabulated in Table 3. The longitudinal coverage is total and the latitudinal coverage goes from −60° to +60° planetocentric latitudes.

4.3. Short-term variations

Different wind profiles were obtained on several dates with differences in wind values noted at particular latitudes. To know if these changes represent real short-term changes in the zonal winds structure, the magnitude of the wind variation must be carefully compared with the wind measurement error. We clustered the image pairs into three small sets around the same dates and in periods of time that showed few morphological or phenomenological changes. These sets correspond to the following
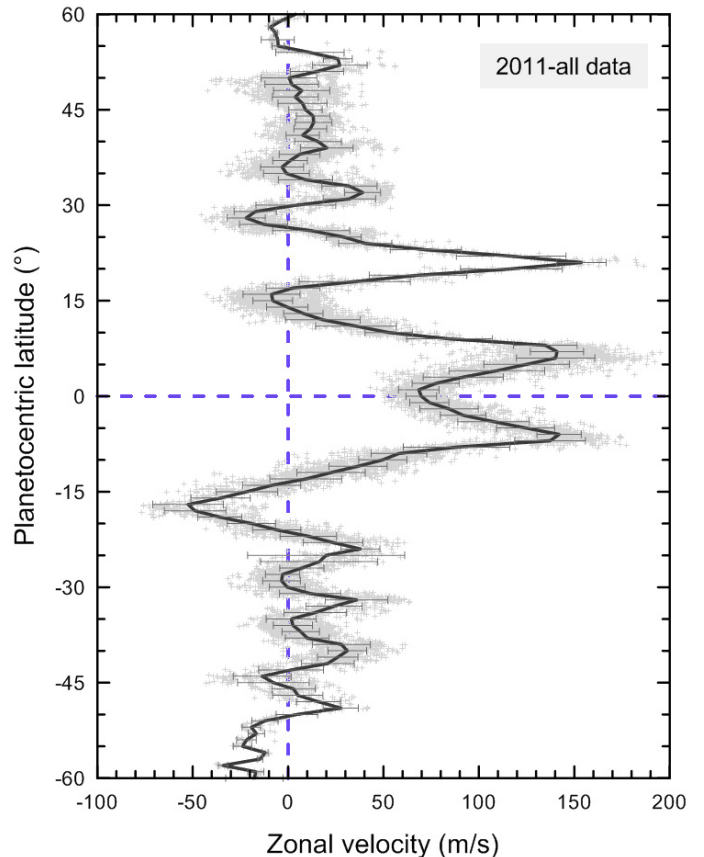
Fig. 5. Jupiter zonal wind profile retrieved from the 23 image pairs analyzed. Individual measurements are represented as dots. The black line is the mean value of the velocity binned in 1° latitude boxes. Error bars represent the standard deviation of the wind value in each bin.
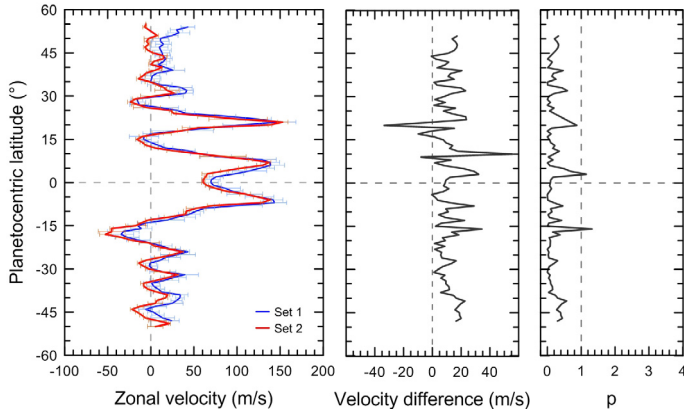
Fig. 6. Comparison between the winds retrieved on September 23−27 (Set 1) with those obtained on October 23−24 (Set 2). In *the middle panel*, the difference in velocity between both profiles is represented, and in *the right panel*, the *p* parameter measuring the statistical significance of the wind velocity variations is shown.
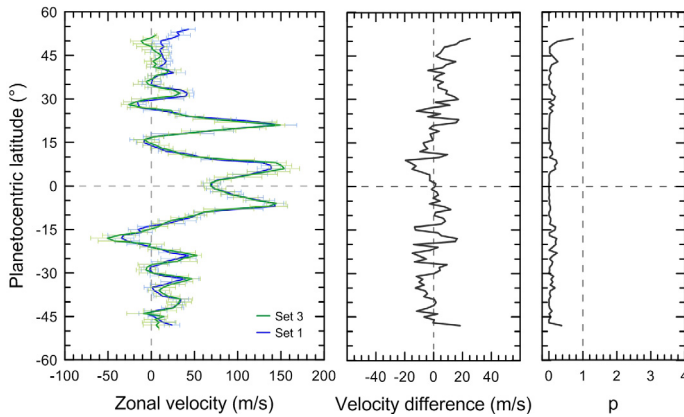
Fig. 7. Same as Fig. 6 but comparing 23−27 September (Set 1) with 13−14 December (Set 3).

periods: a) from September 23 to 27; b) from October 23 to 24; and c) from December 13 to 14. The mean wind profile for each period is shown in Figs. 6−8. Differences between the wind profiles are also shown together with an uncertainty parameter *p* that determines the significance of any detected change. We define this parameter as

$$p = \frac{(u_1 - u_2)^2}{(\sigma_1 + \sigma_2)^2}, \qquad (3)$$

where u_1 and u_2 are the zonal wind velocities of each of the compared profiles and σ_1 and σ_2 are the standard deviations of each latitude value of the profile obtained from the binning. If $(u_1 - u_2)^2 \geq (\sigma_1 + \sigma_2)^2$, that is, if the *p* parameter is greater than 1, the difference between the profiles is statistically meaningful since the difference between the profiles is larger than the sum of both zonal velocity errors.

Short-term variability is at most latitudes below the measurement error, but signatures of wind variability are found at the NTB and NEB. Variations between our first and second sets of dates (see Fig. 6) are greater than the uncertainty parameter at 3° and −16° planetocentric latitudes. The first change may be caused by a small change in the shape of the equatorial retrograde jet since in the second set the jet shows a slightly wider structure than in the first or third sets of measurements. Nevertheless, this variation represents only a small change in the
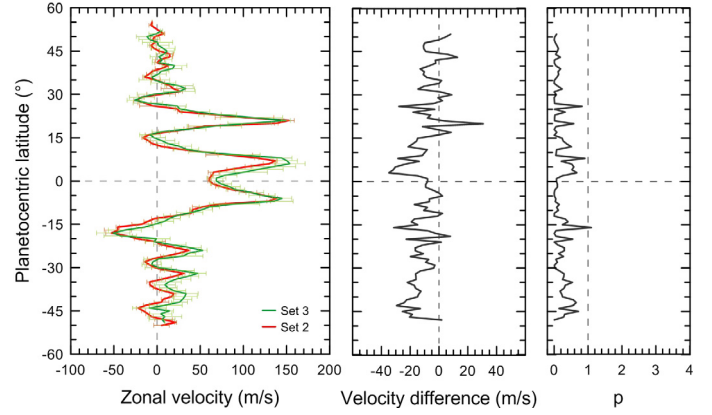
**Fig. 8.** Same as Fig. 6 but comparing 23−24 October (Set 2) with 13−14 December (Set 3).

wind. The other change corresponds to an increase of westward velocity at −16°. This latitude is dominated by the presence of the Great Red Spot and, although we avoided the GRS itself, its influence in the surrounding longitudes may perturb the motion of the cloudy features passing through the area close to the GRS. Variations between the second and third sets show a small value of the uncertainty parameter for all latitudes and short-term changes are not detected, as can be observed in Fig. 7. Finally, in Fig. 8, the comparison between our first and third sets shows a similar result to the comparison between the first and second sets. There is a noteworthy difference at −16°, which appears to be a change in the shape of the profile in the area next to the northward edge of the GRS.

4.4. Long-term variations

Here we compare the mean wind profile obtained from the ensemble of all our measurements during 2011 with previous wind profiles of Jupiter retrieved during several years. We compare the 2011 wind profile with those obtained using HST data from 1995 to 1998 (García-Melendo & Sánchez-Lavega 2001), the Cassini wind profile corresponding to late 2000 (Porco et al. 2003), and the most recent one retrieved from HST 2008 observations (Asay-Davis et al. 2011). Figure 9 shows these global wind profiles.

Each wind profile was measured by different authors using slightly different methodologies, but all of them are based on the ensemble of a large number of measurements, have removed the effects of large-scale structures, and have associated retrieval errors in terms of standard deviations of wind measurements. In these high-resolution datasets the standard deviations are always larger than the navigation uncertainties. It is evident from Fig. 9 that some changes at particular latitudes have occurred over the long time scale represented by this data. The most notorious changes happen in the northern hemisphere. There is a large wind variation at the NEB (at 7°), the latitude of the dark projections and corresponding infrared hot spots, at the westward jet at 15°, and at the narrowest and strongest jet of the planet situated at the NTB (at 18°). Another appreciable change is present at the 28° westward jet as discussed by Asay-Davis et al. (2011).

Differences between these wind profiles are examined in further detail in Figs. 10 and 11, where we also show the significance of wind differences using the *p* parameter. The most meaningful change appears at the NEB around 7°N, where the eastward zonal jet has its maximum value and the cloud morphology is dominated in some years by the dark projections and
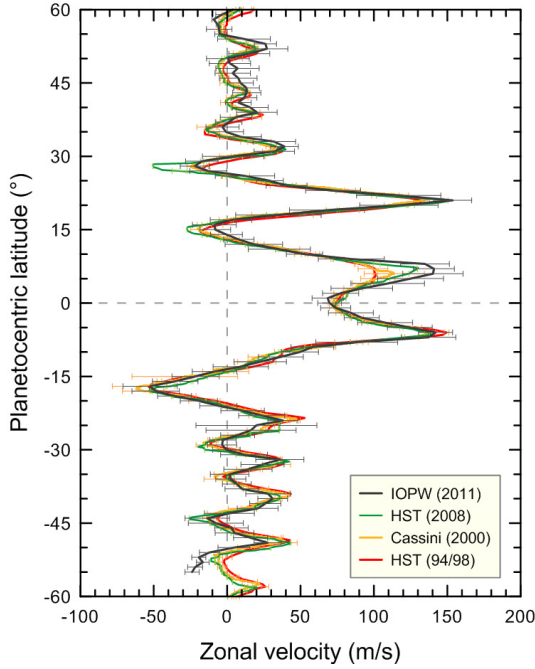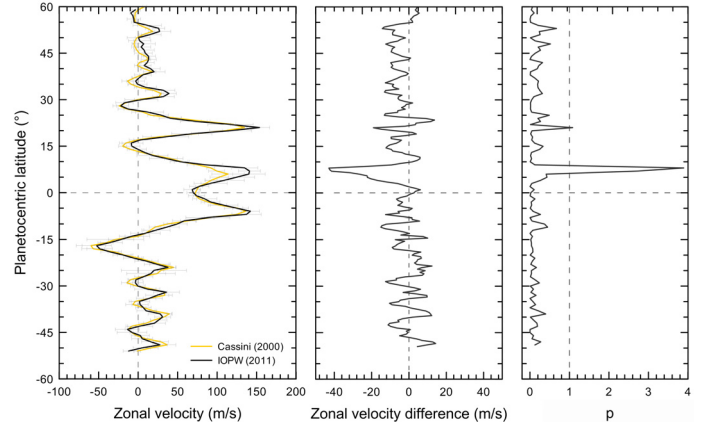
Fig. 9. Jupiter wind profiles in different years. Red line: mean wind profile retrieved by (García-Melendo & Sánchez-Lavega 2001) from HST observations in the period 1994 to 1998. Yellow line: wind profile from the Cassini flyby in 2000 (Porco et al. 2003). Green line: HST observations in 2008 (Asay-Davis et al. 2011). Black line: this work.
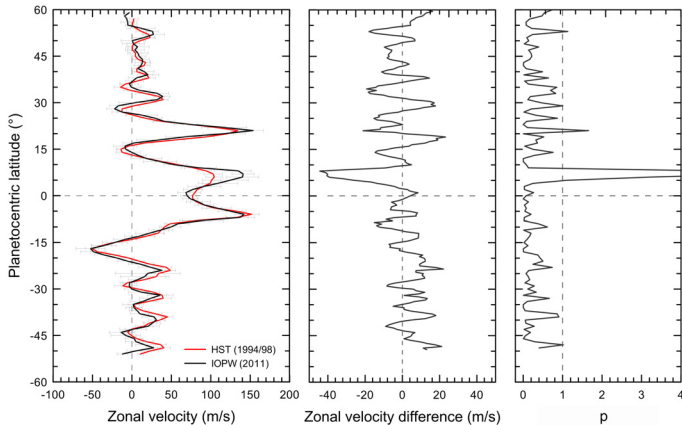

Fig. 10. Comparison between the mean Jupiter profile obtained from the 1994 to 1998 wind profile using HST images (García-Melendo & Sánchez-Lavega 2001) and the 2011 wind profile from this work. *Left panel shows the wind profiles; the middle panel shows the difference between both profiles; the right panel shows the p parameter.*

Fig. 11. Same as in Fig. 10 but comparing the 2000 Cassini wind profile (Porco et al. 2003) with results from this work.
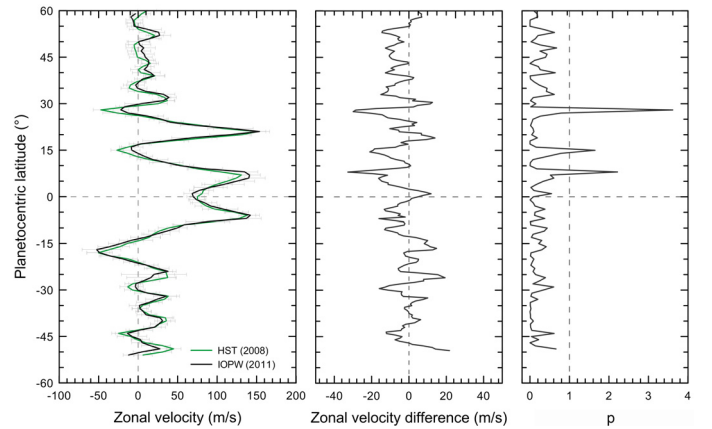
Fig. 12. Same as in Figs. 10 and 11 comparing 2008 HST wind profile (Asay-Davis et al. 2011) with results from this work.

hot spots. Concerns over the zonal wind measurements at this latitude have been raised in the literature since 1996 (Beebe et al. 1996) because most wind profiles are based on the movements of the large-scale dark projections, which could be a manifestation of an equatorial wave (Showman & Dowling 2000). As such, the NEB jet appears to be slower in the period 1995−1998 (HST) and in 2000 (Cassini epoch), when large dark projections and plumes covered most of the NEB dominating the wind profile measurements. However, small-scale cloud features observed in Cassini high-resolution images reproduce the fast velocity characteristics of the NEB when the dark projections are absent (Li et al. 2006; Choi et al. 2013). In 2008 and 2011, which were years with less contrasted dark projections and absences

of equatorial hot spots, the measured jet velocity is found to be faster and similar to its southern counterpart (Fig. 12). In fact the drift rate of the equatorial dark projections matches a Rossby wave dispersion relationship as described in García-Melendo et al. (2011a).

Another significant difference appears around 21° North when we compare the 2011 profile with the 1995−1998 averaged and 2000 profiles (Figs. 10 and 11). This is the latitude of the NTB, where the fastest jet stream lies and where planetary-scale convective disturbances (NTBD) developed with some recurrence (Sánchez-Lavega et al. 1990; García-Melendo et al. 2005), the last one having occurred in 2007 (Sánchez-Lavega et al. 2008; Barrado-Izagirre et al. 2009a).

Wind differences are less significant when we compare the situation in 2008 to the 2011 data (Fig. 12). This is a reasonable result not only because of the smaller time difference between both profiles but also because of the visual appearance of the cloud morphology in both years. The appearance is very similar despite recent large-scale cyclic variations such as the Fade (2009−10) and Revival (2010) of the SEB (Pérez-Hoyos et al. 2012; Fletcher et al. 2011) or the impact of a 500 m object with Jupiter in 2009 at −55° latitude (Sánchez-Lavega et al. 2010), which resulted in a large dark debris cloud that moved at the same velocity as the general flow as retrieved from HST (Hammel et al. 2010) and ground-based observations (Sánchez-Lavega et al. 2011). The only notorious change between these two epochs occurred at latitude 27−28°, where 2008 HST data showed a westward acceleration of the

jet (Asay-Davis et al. 2011). From our current analysis, the jet slowed down after that year and in 2011 acquired the same values as in previous years.

5. Conclusions

We have shown that ground-based images of Jupiter obtained with small telescopes (30−50 cm) employing the lucky imaging method can be used to retrieve regularly the Jovian zonal wind profile with good spatial resolution. We demonstrate that an image correlation technique can be successfully used to measure winds in Jupiter after careful selection of images obtained by amateur astronomers and appropriate navigation. The main results of this work are the validation of the amateur data and measurement technique used to retrieve the wind profile at cloud level and the mean 2011 wind profile shown in Fig. 5. These measurements also demonstrate the capability to monitor possible variations in Jovian jets and to establish the temporal scales involved and the relationship to morphology changes. Accordingly, in the period from September to December 2011, the detected short-term changes in the wind profile are within the measurement uncertainties without noteworthy changes. The 2011 Jovian wind profile presents interesting changes above the statistical errors when compared with profiles obtained from higher quality images over previous years at some particular latitudes. The most significant is the wind variation that occurred in the NEB linked to the different morphology of this belt. When the visual dark projections related to the infrared hot spots are present, their lower velocity, which is possibly due to their relationship to a Rossby wave (Arregi et al. 2006; García-Melendo et al. 2011a), dominates the wind retrievals in the whole NEB. When these large-scale features are not present, the measured winds appear larger and symmetric with the SEB jet, possibly corresponding to the true velocity of the jet. Implementations of the lucky imaging observations of Jupiter with 1−2 m size telescopes (Śanchez-Lavega et al. 2012) will result in better capabilities in the future to study the overall dynamics of the Jovian atmosphere and its variable phenomena using the regular and extended coverage provided by ground-based amateur observations.

References

Arregi, J., Rojas, J. F., Sánchez-Lavega, A., & Morgado, A. 2006, J. Geophys. Res. (Planets), 111, 9010
Asay-Davis, X. S., Marcus, P. S., Wong, M. H., & de Pater, I. 2011, Icarus, 211, 1215
Atkinson, D. H., Pollack, J. B., & Seiff, A. 1998, J. Geophys. Res., 103, 22911
Barrado-Izagirre, N., Pérez-Hoyos, S., Garcıa-Melendo, E., & Sánchez-Lavega, A. 2009a, A&A, 507, 513
Barrado-Izagirre, N., Pérez-Hoyos, S., & Sánchez-Lavega, A. 2009b, Icarus, 202, 181
Barrey, R. F. T. 1984, A Users Guide to Voyager Image Processing (London: Atmospheric Physics Group, The Blackett Laboratory, Imperial College)
Beebe, R. F., Orton, G. S., & West, R. A. 1989, NASA Spec. Publ., 494, 245
Beebe, R. F., Simon, A. A., & Huber, L. F. 1996, Science, 272, 841
Cano, J. 1998, L.A.I.A. Laboratorio de Análisis de Imágenes Astronómicas (Spain, Barcelona: Grup d'Estudis Astronómics)
Chapman, C. R., & Reese, E. J. 1968, Icarus, 9, 326
Choi, D. S., Showman, A. P., Vasavada, A. R., & Simon-Miller, A. A. 2013, Icarus, 223, 832
Dowling, T. E. 1995, Icarus, 117, 439
Dowling, T. E., & Ingersoll, A. P. 1989, J. Atmos. Sci., 46, 3256
Fletcher, L. N., Orton, G., Rogers, J., et al. 2011, Icarus, 213, 564
García-Melendo, E., & Sánchez-Lavega, A. 2001, Icarus, 152, 316
García-Melendo, E., Sánchez-Lavega, A., & Dowling, T. E. 2005, Icarus, 176, 272
García-Melendo, E., Legarreta, J., Sánchez-Lavega, A., et al. 2009, Icarus, in press
García-Melendo, E., Arregi, J., Rojas, J. F., et al. 2011a, Icarus, 211, 1242
García-Melendo, E., Pérez-Hoyos, S., Sánchez-Lavega, A., & Hueso, R. 2011b, Icarus, 215, 62
Hammel, H. B., Beebe, R. F., Ingersoll, A. P., et al. 1995, Science, 267, 1288
Hammel, H. B., Wong, M. H., Clarke, J. T., et al. 2010, ApJ, 715, L150
Horak, H. G. 1950, ApJ, 112, 445
Hueso, R., Legarreta, J., García-Melendo, E., Sánchez-Lavega, A., & Pérez-Hoyos, S. 2009, Icarus, 203, 499
Hueso, R., Legarreta, J., Pérez-Hoyos, S., et al. 2010, Planet. Space Sci., 58, 1152
Ingersoll, A. P., Dowling, T. E., Gierasch, P. J., et al. 2004, in Jupiter. The Planet, Satellites and Magnetosphere, 105
Li, L., Ingersoll, A. P., Vasavada, A. R., et al. 2006, Icarus, 185, 416
Limaye, S. S. 1986, Icarus, 65, 335
Minnaert, M. 1941, ApJ, 93, 403
Minton, R. B. 1972a, Commun. Lun. Planet. Lab., 9, 361
Minton, R. B. 1972b, Commun. Lun. Planet. Lab., 9, 397
Parker, D. 2007, Sky & Telescope, 113, 129
Peek, P. M. 1958, The planet Jupiter (London: Faber and Faber)
Pérez-Hoyos, S., Sanz-Requena, J. F., Barrado-Izagirre, N., et al. 2012, Icarus, 217, 256
Petrou, M., & Petrou, C. 2010, Image Processing: The fundamentals (West Susssex, UK: John Wiley & Sons Ltd)
Porco, C. C., West, R. A., McEwen, A., et al. 2003, Science, 299, 1541
Reese, E. J. 1972, Icarus, 17, 57
Reuter, D. C., Simon-Miller, A. A., Lunsford, A., et al. 2007, Science, 318, 223
Rogers, J. H. 1995, The giant planet Jupiter (Cambridge; New York, Cambridge University Press)
Sánchez-Lavega, A., & Gómez, J. M. 1996, Icarus, 121, 1
Sanchez-Lavega, A., & Rodrigo, R. 1985, A&A, 148, 67
Sanchez-Lavega, A., Laques, P., Parker, D. C., & Viscardy, G. 1990, Icarus, 87, 475
Sanchez-Lavega, A., Gomez, J. M., Lecacheux, J., et al. 1996, Icarus, 121, 18
Sanchez-Lavega, A., Gomez, J. M., Rojas, J. F., et al. 1998, Icarus, 131, 341
Sanchez-Lavega, A., Rojas, J. F., & Sada, P. V. 2000, Icarus, 147, 405
Sánchez-Lavega, A., Orton, G. S., Hueso, R., et al. 2008, Nature, 451, 437
Sánchez-Lavega, A., Wesley, A., Orton, G., et al. 2010, ApJ, 715, L155
Sánchez-Lavega, A., Orton, G. S., Hueso, R., et al. 2011, Icarus, 214, 462
Sanchez-Lavega, A., Rojas, J. F., Hueso, R., et al. 2012, Ground-based and Airborne Instrumentation for Astronomy IV, Proc. SPIE 8446, 84467X1
Showman, A. P., & Dowling, T. E. 2000, Science, 289, 1737
Simon-Miller, A. A., & Gierasch, P. J. 2010, Icarus, 210, 258
Simon-Miller, A. A., Poston, B. W., Orton, G. S., & Fisher, B. 2007, Icarus, 186, 192
Simon-Miller, A. A., Rogers, J. H., Gierasch, P. J., et al. 2012, Icarus, 218, 817
Smith, B. A., & Hunt, G. E. 1976, in Jupiter: Studies of the Interior, Atmosphere, Magnetosphere and Satellites, ed. T. Gehrels, IAU Colloq., 30, 564
Sromovsky, L. A., Fry, P. M., Dowling, T. E., Baines, K. H., & Limaye, S. S. 2001, Icarus, 149, 459
Sromovsky, L. A., Fry, P. M., Hammel, H. B., et al. 2009, Icarus, 203, 265
Vasavada, A. R., & Showman, A. P. 2005, Rep. Prog. Phys., 68, 1935
Vasavada, A. R., Ingersoll, A. P., Banfield, D., et al. 1998, Icarus, 135, 265
Walker, S. 2013, in Sky Telescope, 125, ed. R. Naeye, 70

Table 2. IOPW team's observations.

Date	Time	Observer	Telescope diam. (mm)
2011-08-31	03:24	Javier Beltran Jovani	
2011-08-31	03:57	Marco Guidi	
2011-08-31	04:29	Michael Jackesson	203
2011-08-31	04:46	Javier Beltran Jovani	
2011-08-31	14:05	Freddy Willems	356
2011-09-01	00:34	Dave Tyler	356
2011-09-01	09:53	Brian Combs	356
2011-09-01	19:56	Trevor Barry	
2011-09-03	01:08	Dave Tyler	356
2011-09-13	07:14	Brian Combs	356
2011-09-13	08:04	Brian Combs	356
2011-09-13	18:06	Brian Combs	356
2011-09-14	02:21	Damian Peach	350
2011-09-23	03:25	Damian Peach	350
2011-09-24	00:14	Damian Peach	350
2011-09-24	13:43	Freddy Willems	356
2011-09-25	01:20	Emil Kraaikamp	400
2011-09-25	21:58	Jordi Ortega	280
2011-09-27	07:01	Efrain Morales	300
2011-09-28	02:54	Damian Peach	350
2011-09-30	05:35	Brian Coms	356
2011-10-01	00:51	Dave Tyler	356
2011-10-01	05:34	Efrain Morales	300
2011-10-01	23:53	Emil Kraaikamp	400
2011-10-02	00:36	Damian Peach	350
2011-10-02	05:54	Efrain Morales	300
2011-10-03	02:36	Damian Peach	350
2011-10-05	09:18	Brian Combs	356
2011-10-06	05:44	Brian Combs	356
2011-10-14	02:15	Pic du Midi	1050
2011-10-14	22:16	Pic du Midi	1050
2011-10-15	18:27	Pic du Midi	1050
2011-10-23	04:51	Brian Combs	356
2011-10-23	05:49	Wayne Jaeschke	356
2011-10-23	14:47	Tomio Akutsu	356
2011-10-24	01:58	Efrain Morales	300
2011-10-31	22:11	Cristian Fattinnanzi	360
2011-10-31	23:14	Damian Peach	350
2011-11-01	08:29	Freddy Willems	356
2011-11-01	19:18	Manos Kardasis	280
2011-11-18	00:00	Damian Peach	350
2011-11-18	20:49	Damian Peach	350
2011-11-29	12:20	Christopher Go	280
2011-11-29	21:22	Jesús Ránchez	
2011-12-14	01:51	Ian Sharp	280
2011-12-14	02:03	Ian Sharp	280
2011-12-14	02:20	Ian Sharp	280
2011-12-14	12:19	Christopher Go	280
2011-12-14	12:07	Christopher Go	280
2011-12-14	12:30	Christopher Go	280
2011-12-14	22:15	Ian Sharp	280

Notes. http://www.pvol.ehu.es/pvol/

Table 3. Averaged mean zonal winds from IOPW observations in 2011.

φ (°)	$\langle u \rangle$ (m/s)	σ (m/s)	n
63.0	6.51	15	2
62.0	7.17	15	5
61.0			
60.0	3.99	15	8
59.0	−3.48	4.24	14
58.0	−9.17	1.13	10
57.0	−6.54	0.96	10
56.0	−5.41	8.68	11
55.0	−5.22	3.17	17
54.0	11.44	17.93	19
53.0	26.09	7.56	27
52.0	27.09	14.26	47
51.0	15.10	13.95	91
50.0	0.51	14.55	145
49.0	1.89	14.06	223
48.0	7.09	14.73	201
47.0	3.78	12.03	216
46.0	7.55	12.84	129
45.0	9.10	8.75	55
44.0	13.15	8.84	82
43.0	13.35	9.60	212
42.0	11.61	8.62	326
41.0	7.64	8.71	285
40.0	15.69	12.27	185
39.0	20.26	13.80	215
38.0	6.02	10.69	328
37.0	1.01	9.04	351
36.0	−3.17	11.27	224
35.0	−0.87	12.01	282
34.0	9.14	14.22	212
33.0	32.13	14.46	227
32.0	39.05	9.42	253
31.0	32.13	13.76	259
30.0	4.06	20.91	119
29.0	−17.22	11.06	133
28.0	−21.96	9.99	138
27.0	−12.86	12.62	198
26.0	12.13	20.21	251
25.0	29.14	9.09	220
24.0	40.46	13.93	87
23.0	72.22	18.68	38
22.0	116.92	28.73	38
21.0	153.67	13.00	39
20.0	117.05	26.68	37
19.0	68.02	25.51	70
18.0	34.93	29.13	132
17.0	2.62	14.11	173
16.0	−8.71	14.91	466
15.0	−8.04	10.41	601
14.0	−0.45	10.85	563
13.0	7.98	10.32	521
12.0	18.20	19.59	467
11.0	35.55	21.18	194
10.0	52.72	12.36	136
9.0	84.61	22.47	90
8.0	134.82	16.65	289
7.0	140.91	13.95	737
6.0	140.22	20.56	517
5.0	125.00	22.42	289
4.0	109.39	25.06	220
3.0	91.80	20.99	224

Notes. φ is the planetocentric latitude, σ the standard deviation and n the number of measured vectors.

Table 3. continued.

φ	$\langle u \rangle$	σ	n
(°)	(m/s)	(m/s)	
2.0	77.33	12.29	192
1.0	68.48	10.61	230
0.0	69.79	8.03	286
−1.0	74.00	10.24	284
−2.0	84.33	15.30	259
−3.0	91.69	11.95	176
−4.0	107.69	18.75	173
−5.0	124.48	15.24	209
−6.0	142.05	11.59	293
−7.0	137.30	18.50	258
−8.0	88.31	27.90	181
−9.0	58.09	14.56	270
−10.0	49.63	12.63	465
−11.0	36.65	15.24	370
−12.0	22.53	17.87	295
−13.0	9.27	18.82	208
−14.0	−8.59	15.17	197
−15.0	−21.51	16.06	161
−16.0	−35.39	15.52	54
−17.0	−52.47	18.50	70
−18.0	−48.74	16.12	112
−19.0	−35.83	11.52	143
−20.0	−19.27	12.68	182
−21.0	−5.97	12.66	218
−22.0	10.57	14.79	274
−23.0	23.53	15.66	133
−24.0	37.94	10.20	41
−25.0	19.95	41.18	86
−26.0	16.27	30.68	78
−27.0	7.18	11.57	186
−28.0	−2.91	8.97	203
−29.0	−3.45	9.91	182
−30.0	−0.46	9.32	273
−31.0	11.49	15.97	239
−32.0	35.92	16.37	169
−33.0	24.11	14.68	69
−34.0	14.19	16.43	119
−35.0	1.65	13.12	109
−36.0	2.51	10.25	290
−37.0	6.62	9.82	389
−38.0	10.04	11.49	218
−39.0	27.93	15.21	142
−40.0	31.03	10.12	233
−41.0	25.98	10.56	228
−42.0	20.79	13.88	121
−43.0	1.54	16.99	61
−44.0	−13.58	15.14	74
−45.0	−7.75	18.74	63
−46.0	2.90	11.38	60
−47.0	5.02	13.22	43
−48.0	15.93	11.56	33
−49.0	27.58	9.23	16
−50.0	4.60	10.86	15
−51.0	−12.08	6.84	15
−52.0	−19.33	4.78	15
−53.0	−16.61	4.31	12
−54.0	−21.82	5.09	13
−55.0	−23.91	4.82	10
−56.0	−12.10	1.55	10
−57.0	−14.62	15	6
−58.0	−34.14	15	8
−59.0	−16.93	4.25	10
−60.0	−17.69	15	5